THE ASTROPHYSICAL JOURNAL, 349:107–119, 1990 January 20

STUDIES OF DUST GRAIN PROPERTIES IN INFRARED REFLECTION NEBULAE

Y. J. PENDLETON,[1] A. G. G. M. TIELENS,[1] AND M. W. WERNER[1]
NASA Ames Research Center
Received 1989 February 27; accepted 1989 July 19

ABSTRACT

We have developed a model for reflection nebulae around luminous infrared sources embedded in dense dust clouds. The aim of this study is to determine the sizes of the scattering grains. In our analysis, we have adopted an MRN-like power-law size distribution (Mathis, Rumpl, and Nordsieck) of graphite and silicate grains, but other current dust models would give results which were substantially the same. In the optically thin limit, the intensity of the scattered light is proportional to the dust column density, while in the optically thick limit, it reflects the grain albedo. The results show that the shape of the infrared spectrum is the result of a combination of the scattering properties of the dust, the spectrum of the illuminating source, and foreground extinction, while geometry plays a minor role. Comparison of our model results with infrared observations of the reflection nebula surrounding OMC-2/IRS 1 shows that either a grain size distribution like that found in the diffuse interstellar medium, or one consisting of larger grains, can explain the observed shape of the spectrum. However, the absolute intensity level of the scattered light, as well as the observed polarization, requires large grains ($\sim$5000 Å).

By adding water ice mantles to the silicate and graphite cores, we have modeled the 3.08 μm ice band feature, which has been observed in the spectra of several infrared reflection nebulae. We show that this ice band arises naturally in optically thick reflection nebulae containing ice-coated grains. We show that the shape of the ice band is diagnostic of the presence of large grains, as previously suggested by Knacke and McCorkle. Comparison with observations of the BN/KL reflection nebula in the OMC-1 cloud shows that large ice grains ($\sim$5000 Å) contribute substantially to the scattered light.

Subject headings: infrared: sources — infrared: spectra — interstellar: grains — nebulae: reflection

I. INTRODUCTION

It is well known that the properties of interstellar dust inside dense molecular clouds differ from those of dust in the diffuse interstellar medium. Extinction observations show that the ratio $R = A_V/E_{B-V}$ is larger in molecular clouds than in the diffuse medium. This is generally taken to imply a larger mean grain size in such regions. Likewise, the wavelength where polarization reaches maximum, λ_{max}, is larger in dense molecular clouds than in the diffuse interstellar medium, again indicating a large grain size (see Savage and Mathis 1979 for review). These two measures of grain size correlate very well, further strengthening this conclusion. An increase in the average grain size will have a pronounced influence on the scattering properties of the dust, a question that we investigate in this study. Two processes which would account for larger grain size are grain coagulation and the growth of ice mantles (Jura 1980; Tielens 1989).

Classical reflection nebulae, such as NGC 2023 and the Merope nebula, have been studied extensively at visual and near-infrared wavelengths (see Witt 1989 and Sellgren 1989, for recent review). In this study, we concentrate on infrared reflection nebulae, dusty regions in dense molecular clouds that are illuminated by embedded infrared sources. Recent observations have shown that infrared reflection nebulae are common in star-forming regions (Tokunaga, Lebofsky, and Rieke 1981; Werner, Dinerstein, and Capps 1983; Lenzen, Hodapp, and Solf 1984; Pendleton *et al.* 1986) and that the bulk of the near-infrared (1–5 μm) radiation in many such regions is scattered light. Detailed observational studies of such reflection nebulae have revealed important information on the spatial structure of star-forming regions (Werner, Dinerstein, and Capps 1983). Such studies can also be used to constrain the scattering properties of the reflecting dust. The latter is the goal of this article. We present comparisons of theoretical models of infrared reflection nebulae to infrared observations of reflection nebulae in the Orion molecular cloud 1 (OMC-1) and Orion molecular cloud 2 (OMC-2), demonstrating the usefulness of infrared reflection nebulae as probes of dust grain properties in regions of star formation. Similar theoretical studies of visual reflection nebulae have been undertaken by, among others, Witt (1977), White (1979), and Sellgren (1984).

The goal of this study is to determine the dust properties in infrared reflection nebulae. The approach is twofold: (1) model the overall brightness and shape of the near-infrared spectra of infrared reflection nebulae and (2) investigate the effects of scattering on the 3.08 μm ice absorption band, a feature which has been detected toward protostellar sources and is seen in infrared reflection nebulae. The 3.08 μm feature is commonly attributed to absorption by water ice; however, the presence of NH_3 has also been inferred from a 2.9 μm wing on the H_2O ice band which has been detected toward some deeply embedded objects (Knacke *et al.* 1982). Scattering by large water ice particles can also produce an apparent absorption feature at $\sim$2.9 μm, and has been put forth as an alternative explanation for this wing (Knacke and McCorkle 1987). We present further evidence supporting this suggestion as well as arguments which demonstrate that, in both OMC-1 and OMC-2, the infrared reflection nebulae appear to contain grains which are larger than grain sizes typical of the interstellar medium. Rouan and Leger (1984) arrived at a similar conclusion for the

[1] Visiting Astronomer at the Infrared Telescope Facility, which is operated by the University of Hawaii under contract from the National Aeronautics and Space Administration.

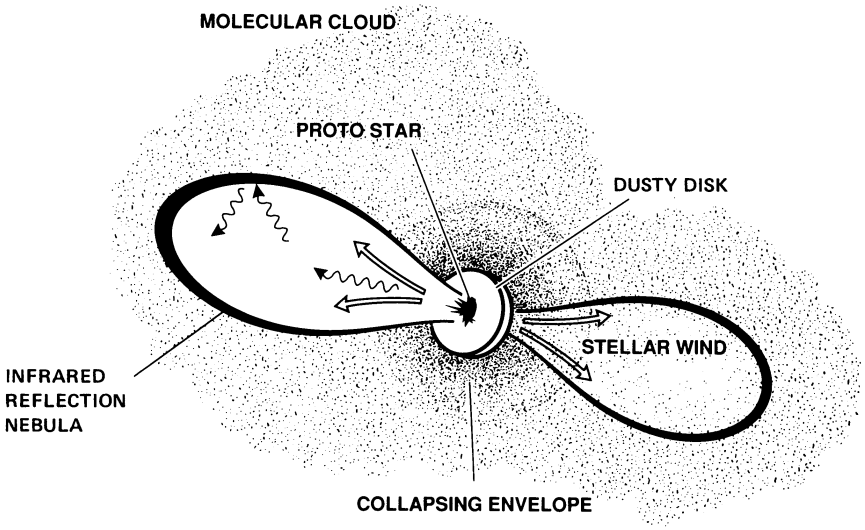

FIG. 1.—Possible scenario for the formation of an infrared reflection nebula around a protostar, where the strong stellar wind has blown a large cavity around the central illuminating object.

grains in the BN/KL reflection nebula, based on an analysis of the observed intensity and degree of polarization of the scattered light. Recent work by Yamashita *et al.* (1989) also suggests the presence of large grains in the infrared reflection nebulae associated with GL 490 and R Mon.

In § II we present our model and derive simple formulae describing the reflected intensity from an infrared reflection nebula. In § III, the parameters of the dust model are presented. We discuss the impact of multiple scattering on the model based on an analysis of isotropic scattering in regions of high optical depth. Section IV contains results of a parameter space study which covers variations in geometry and in grain properties. Applications to infrared reflection nebulae in OMC-1 and OMC-2 are presented in § V. Conclusions are given in § VI.

II. SCATTERING NEBULA

We have calculated the near-infrared spectrum of the light scattered by grains in infrared reflection nebulae. The physical model assumed in this work is shown in Figure 1, which is a possible scenario for the formation of an infrared reflection nebula around a protostar. In this picture, first suggested by Downes *et al.* (1981) for the KL nebula in the OMC-1 region, part of a molecular cloud collapses to form a protostar. Because angular momentum is conserved during the collapse, a dusty disk is formed around the central protostar. A strong stellar wind from the newly formed star will create a large cavity around the central object and will sweep up the surrounding molecular cloud material into two lobes. In such an asymmetric density distribution, stellar photons, either direct or reprocessed by the disk, can escape more freely along the poles than through the equatorial plane. The material in the lobes forms the infrared reflection nebula where photons from the central illuminating source are scattered toward the observer.

Our study has focused on the 1–5 μm region in order to model the overall shape and brightness of the near-infrared energy distributions in reflection nebulae. We have used graphite, silicate, and water ice grains to model the near-infrared absorption and scattering produced by interstellar grains (see § III). The reflection nebula is represented by a plane-parallel slab which scatters starlight, I_0, incident at an angle θ_0, through a total angle, ϕ, to produce the observed scattered light, I_s (Fig. 2). Note that, by convention, forward scattering ($\theta = 0°$) corresponds to the direction along the incident beam. Thus, in our notation, $\phi = 180° - (\theta + \theta_0)$. The extinction optical depth for normal incidence of the slab is denoted by τ, while the optical depth along the line of sight through the nebula is given by τ_L, thus, $\tau = \tau_L \cos\theta$.

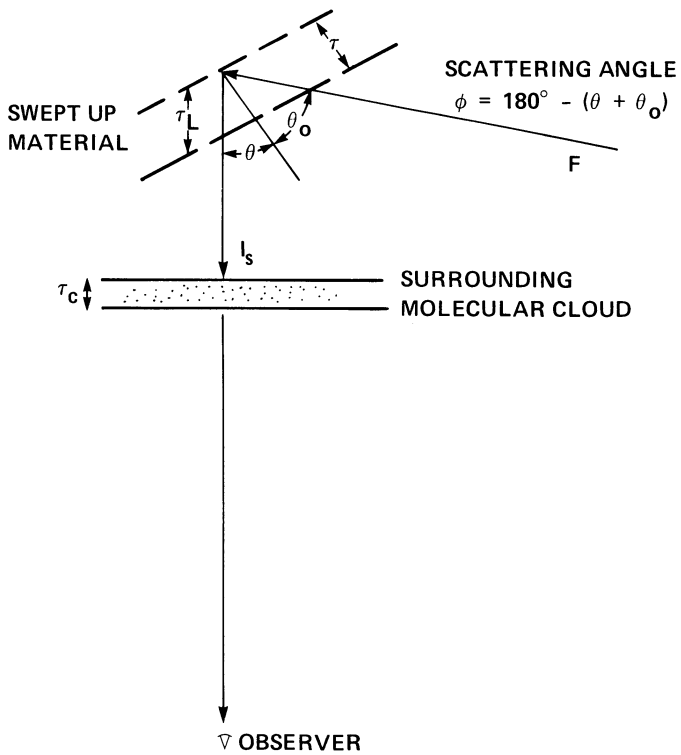

FIG. 2.—Schematic drawing of the geometry used in our model. The nebula is locally approximated by a plane-parallel slab. Optical depth along our line of sight is given by τ_L and is related to the optical depth of the slab by $\tau = \tau_L \cos\theta$, where $\phi = 180° - (\theta + \theta_0)$ represents the total scattering angle. The incident angle and incident flux are given by θ_0 and πF, respectively. Additional extinction from circumstellar material or foreground extinction may contribute an amount τ_c to the total extinction.

Consider a parallel beam of radiation of net flux πF per unit area which illuminates a plane-parallel slab of optical depth τ at an angle θ_0. The angular distribution of the diffusely reflected intensity, $I_s(\tau, \mu)$, at the surface ($\tau = 0$) in the direction θ, can be expressed in terms of a scattering function, $\mathscr{S}(\mu, \mu_0)$, such that

$$I_s(0, \mu) = \frac{F}{4\mu} \mathscr{S}(\mu, \mu_0) \quad 0 \le \mu \le 1 , \tag{1}$$

where $\mu = \cos \theta$ and $\mu_0 = \cos \theta_0$ (Chandrasekhar 1960) as shown in Figure 2. If the nebula is illuminated by a star of temperature T_*, and radius R_*, which is a distance $d_{\rm neb}$ from the nebula, F is given by

$$F = \left(\frac{R_*}{d_{\rm neb}}\right)^2 B(\lambda, T_*) , \tag{2}$$

where $B(\lambda, T_*)$ is the Planck function. In general, besides the scattering angles, the scattering function, $\mathscr{S}$, is also dependent on the dust-scattering properties and the total optical depth of the slab.

a) *Semi-infinite Atmospheres*

For isotropic scattering in a semi-infinite slab, the scattering function, $\mathscr{S}(\mu, \mu_0)$, is independent of the total optical depth and can be expressed as

$$\mathscr{S}(\mu, \mu_0) = \frac{\mu\mu_0}{\mu + \mu_0} \omega_0 H(\mu) H(\mu_0) , \tag{3}$$

where $H(\mu)$ is the H function (Chandrasekhar 1960) and ω_0 is the average grain albedo (see § III). The scattered intensity is then given by

$$I_s(0, \mu) = F\omega_0 \mu_0 H(\mu) H(\mu_0)/4(\mu + \mu_0) . \tag{4}$$

The $H(\mu)$ functions are given by nonlinear integral equations where

$$H(\mu) = 1 + \tfrac{1}{2}\omega_0 \mu H(\mu) \int_0^1 [H(\mu')/(\mu + \mu')] d\mu' . \tag{5}$$

In general, the $H(\mu)$ function depends on the albedo of the scattering material as well as on the scattering angle. For small albedos, these dependences can be factored out such that

$$H(\mu) = 1 + \omega_0 f(\mu) , \tag{6}$$

so that $f(\mu)$ contains the geometrical factors. The integral equation for $H(\mu)$ can then be solved to give

$$H(\mu) = 1 + \frac{\omega_0 \mu}{2} \ln\left(1 + \frac{1}{\mu}\right) . \tag{7}$$

Comparison with the exact solution for $H(\mu)$ tabulated by Chandrasekhar (1960) shows that this first-order solution is accurate for any μ value to within 25% for albedos less than 0.7. The accuracy ($\le 1\%$) will be much higher for lower albedos ($\omega_0 \le 0.1$), and therefore equation (7) is appropriate for this analysis, because the average grain albedo considered here is at most 0.5 and is generally much less. In the limit of low albedo, the H functions are unity and the spectrum of a semi-infinite scattering nebula reflects the albedo directly, so that

$$I_s(0, \mu) = F\omega_0 \frac{\mu_0}{4(\mu + \mu_0)} . \tag{8}$$

b) *Finite Atmospheres*

For finite atmospheres, the scattering function in equation (1) is given by

$$\mathscr{S}(\mu, \mu_0) = \frac{\mu\mu_0}{\mu + \mu_0} \omega_0 [X(\mu)X(\mu_0) - Y(\mu)Y(\mu_0)] , \tag{9}$$

where for small optical depths ($\tau \le 0.5$), the X- and Y-functions can be approximated by

$$X(\mu) = 1 + \Delta\tau\mu(1 - e^{-\tau/\mu}) , \tag{10}$$

and

$$Y(\mu) = e^{-\tau/\mu} + \Delta\tau\mu(1 - e^{-\tau/\mu}) . \tag{11}$$

The functions $X(\mu)$ and $Y(\mu)$ are related to the reflected and transmitted radiation components, respectively (Chandrasekhar 1960). The expression for $\Delta\tau$ is given by

$$\Delta\tau = \frac{\frac{1}{4}\omega_0\{1 - [E_2(\tau)]^2\}}{[\frac{1}{2} - E_3(\tau)]\{1 - \frac{1}{2}\omega_0[1 - E_2(\tau)]\}} , \tag{12}$$

where E_n is the exponential integral of degree n (Abramowitz and Stegun 1970). For calculations in regions of intermediate optical depth ($0.05 \le \tau \le 0.5$), the scattering function (eq. [9]) will give satisfactory representation. For $\tau \le 0.05$, the optically thin limit suffices; only the first terms in the equations for X and Y need to be taken into account, and the intensity becomes

$$I_s = \frac{F}{4} \frac{\mu_0}{\mu + \mu_0} \omega_0 [1 - e^{-\tau(1/\mu + 1/\mu_0)}]$$

$$= \frac{F\tau_{\rm sca}}{4} . \tag{13}$$

In equation (13), $\tau_{\rm sca}$ is the scattering optical depth along the line of sight given by

$$\tau_{\rm sca}(\lambda) = n_d n_0 C_{\rm sca} L , \tag{14}$$

where n_d is the dust density per H atom, n_0 is the density of H nuclei (i.e., $n_0 = 2n_{\rm H_2} + n_{\rm H}$, where $n_{\rm H_2}$ is the density of H_2 molecules and $n_{\rm H}$ is the hydrogen atom density), $C_{\rm sca}$ is the scattering cross section, and L is the thickness of the slab along our line of sight. Thus, in the optically thin limit, the scattered intensity is proportional to the column density of dust along the line of sight.

c) *Single Scattering Limit*

In the case of low albedo ($\omega_0 \ll 1$), multiple scattering is unimportant, and one can derive an angular-dependent formula for the scattered intensity based on the following general formalism (Pendleton 1987). For single scattering,

$$I_s = \pi F \frac{dC_{\rm sca}}{d\Omega} \int_0^L \exp\left[-\tau\left(1 + \frac{\mu}{\mu_0}\right)\right] dl , \tag{15}$$

where $dC_{\rm sca}/d\Omega$ is the differential scattering cross section and l is measured along the line of sight. This yields

$$I_s = \frac{\pi F}{C_{\rm ext}} \left(\frac{dC_{\rm sca}}{d\Omega}\right)\left(\frac{\mu_0}{\mu + \mu_0}\right)\left\{1 - \exp\left[-\tau_L\left(1 + \frac{\mu}{\mu_0}\right)\right]\right\} , \tag{16}$$

where C_{ext} is the extinction cross section. In the optically thick limit, this reduces to

$$I_s = \frac{\pi F}{C_{ext}}\left(\frac{dC_{sca}}{d\Omega}\right)\left(\frac{\mu_0}{\mu + \mu_0}\right), \quad (17)$$

which, for isotropic scattering (i.e., $dC_{sca}/d\Omega = C_{sca}/4\pi$), reduces to equation (8). In the optically thin limit, we arrive at

$$I_s = \pi F n_d\left(\frac{dC_{sca}}{d\Omega}\right)L . \quad (18)$$

Again, in the isotropic scattering case we recover equation (13). These equations allow estimates of the effects of nonisotropic scattering to be made. When multiple scattering is important and the grain scatters nonisotropically, calculation of the emergent spectrum of a reflection nebula requires a numerical radiative transfer model. Given the current observations and the relatively few possible constraints on such models, development of such a complex model seems unwarranted at present. Moreover, we think that the essential characteristics of infrared reflection nebulae (i.e., dependence of dust grain properties, geometry, etc.) are well represented by our semianalytical model.

d) *Summary of Scattering Nebulae*

Summarizing this discussion, three different optical depth cases are discussed in isotropically scattering nebulae. These are (1) the semi-infinite nebula ($\tau_{sca} \gg 1$), where equation (4) applies; (2) the optically thin atmosphere ($\tau_{sca} \ll 1$), where equation (13) applies; and (3) the intermediate case for a finite atmosphere where equations (9)–(12) apply. When multiple scattering effects are negligible, equations (17) and (18) apply and can be used to study the effects of nonisotropic scattering. Finally, additional extinction, τ_c, due to circumstellar cloud material or foreground material, may also contribute to the total extinction as shown in Figure 2 such that

$$I_{obs} = I_s e^{-\tau_c} , \quad (19)$$

where I_{obs} is the observed intensity. In our models, we will assume that the foreground and nebula dust have the same absorption and scattering properties.

III. DUST MODEL

It is reasonable to assume that the dust in the interstellar medium is characterized by a grain size distribution made up of several different components. Therefore, we consider a grain size distribution in our model. In a grain size distribution, $n(a)$, between upper and lower size limits a_+ and a_-, the average extinction, scattering, and differential scattering cross sections, C_{ext}, C_{sca}, and $dC_{sca}/d\Omega$, are defined by

$$C_{ext} = \frac{1}{n_d}\sum_j \int_{a_-}^{a_+} n(a)C_x(a)da , \quad (20)$$

$$C_{sca} = \frac{1}{n_d}\sum_j \int_{a_-}^{a_+} n(a)C_s(a)da , \quad (21)$$

$$\frac{dC_{sca}}{d\Omega} = \frac{1}{n_d}\sum_j \int_{a_-}^{a_+} n(a)\left[\frac{dC_s(a)}{d\Omega}\right]da , \quad (22)$$

where $C_x(a)$, $C_s(a)$, and $dC_s(a)/d\Omega$ are the Mie extinction, scattering, and differential scattering cross sections of a grain of radius a, where it is understood that the integrals are evaluated for each grain component (i.e., silicate or graphite; see § III*a*) separately and then summed. The grain density is given by

$$n_d = \sum_j \int_{a_-}^{a_+} n(a)da , \quad (23)$$

and the albedo is

$$\omega_0 = C_{ext}/C_{sca} . \quad (24)$$

We can also define the scattering and extinction opacities

$$\bar{\kappa}_{sca} = n_d C_{sca} , \quad (25)$$

and

$$\bar{\kappa}_{ext} = n_d C_{ext} . \quad (26)$$

In general, the differential scattering cross section will be different for light with electric vector parallel and perpendicular to the scattering plane, thus leading to polarization of the scattered light. In the Rayleigh limit, there is a particularly simple relationship between the polarization and the scattering angle

$$P(\phi) = \frac{1 - \cos^2\phi}{1 + \cos^2\phi} \quad (27)$$

($\phi = 180° - [\theta + \theta_0]$; see Fig. 2), and polarization provides direct insight into the geometry of the scattering region. For nonisotropic scattering, the polarization produced by the grain size distribution of particles can be computed for an optically thin (and therefore single scattering) nebula as follows:

$$P = \frac{\sum_j \int_{a_-}^{a_+} (i_\perp - i_\parallel)n(a)da}{\sum_j \int_{a_-}^{a_+} (i_\perp + i_\parallel)n(a)da} , \quad (28)$$

where $i_\parallel$ and $i_\perp$ are the scattered irradiances for incident light polarized parallel and perpendicular to the scattering plane, respectively (Bohren and Huffman 1983). In this notation, the relationship between the irradiances and the differential scattering cross section is given by

$$\frac{dC_{sca}}{d\Omega} = \frac{i_\parallel + i_\perp}{2k^2} , \quad (29)$$

where $k = 2\pi/\lambda$. The intensity of the light with electric vector components scattered parallel to and perpendicular to the scattering plane are $i_\parallel$ and $i_\perp$.

For scattering by a grain size distribution, then, the important dust properties are given by equations (24), (25), and (26).

a) *MRN Distribution*

Although other equally good dust models have been proposed (Greenberg and Chlewicki 1984; Jones, Duley, and Williams 1986), we have chosen the model developed by Mathis, Rumpl, and Nordsieck (1977) (MRN) as an example of a model which works well in the visible and UV portions of the spectrum and which can be readily extrapolated to the near-infrared. In the MRN model, the observed interstellar extinction of starlight is produced by a mixture of graphite and silicate grains with the following power-law distribution of sizes:

$$n_i(a)da = A_i n_H a^{-3.5} da , \quad a_- \le a \le a_+ , \quad (30)$$

where $n_i(a)da$ is the number density of grains of type i with radius in the interval $[a, a + da]$, n_H is the number density of H nuclei, and a is the grain radius. The grain abundances, implicit in the A_i, have been determined by fitting the visible/UV

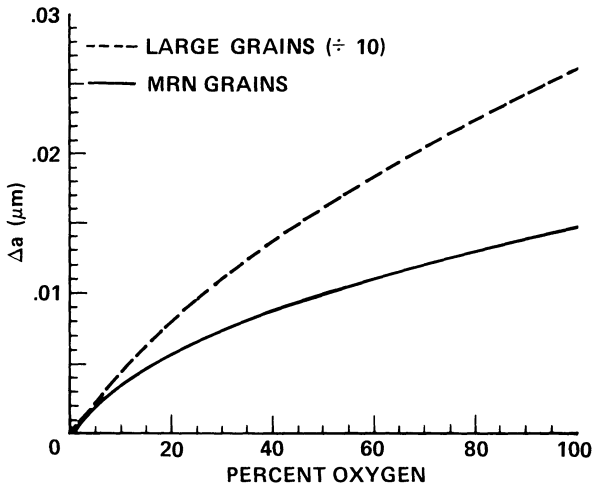

FIG. 3.—Plot of ice mantle thickness, Δa, vs. percentage of oxygen incorporated into the ice for the MRN [$0.005 \leq a(\mu m) \leq 0.25$] and large-grain model [$0.225 \leq a(\mu m) \leq 0.8$]. All size grains receive the same thickness mantle.

extinction curve (Mathis, Rumpl, and Nordsieck 1977). In the models we refer to as MRN, we have adopted the upper and lower cutoffs to the size distribution to be $a_- = 0.005$ μm and $a_+ = 0.25$ μm, where the A_i are $10^{-25.11}$ cm$^{2.5}$/H and $10^{-25.16}$ cm$^{2.5}$/H corresponding to $\sim$60% and $\sim$90% of the available carbon and silicon, respectively, in the form of grains, recently redetermined by Draine and Lee (1984).

b) *Large-Grain Model*

In view of the observational evidence for grain growth in dense molecular clouds, we have explored the effect of varying the grain size limits, holding the power law fixed at -3.5. Although the slope of the grain size distribution may also vary, a full analysis of the effects of coagulation, which would account for a difference in slope, is beyond the scope of this paper. The large grain model case which we explored consisted of grain cores which ranged from 0.225 to 0.8 μm. The upper limit was selected to include grains large enough to demonstrate the contribution of large grain scattering to the ice extinction feature. The lower limit was determined by constraining the total amount of mass contained in the cores constant when going from the MRN to the large case.

c) *Ice Mantles*

Since the rate at which the ice volume of a grain increases is proportional to its surface area (Draine 1985), all grains within the distribution receive the same coating of ice regardless of grain size. For a power-law grain size distribution with index ~ -3.5, small grains dominate the total surface area, and most of the ice is actually on the small grains. Following Draine (1985), the mantle thickness was determined as a function of the percentage of oxygen. The results are shown in Figure 3 for the MRN and large-grain models.

d) *Scattering and Extinction Cross Sections*

Mie scattering cross sections were calculated using the code developed by Bohren and Huffman (1983). The refractive indices ($m = n + ik$) for graphite and silicate in the near-infrared were taken from Draine and Lee (1984), while the refractive indices for 80 K water ice between $2.7 \leq \lambda \leq 3.4$ μm have been measured by Hagen, Tielens, and Greenberg (1983*a*). The optical constants for ice at wavelengths outside this region were taken from the compilation by Warren (1984).

A comparison of the scattering and extinction opacities, $\bar{\kappa}_{sca}$ and $\bar{\kappa}_{ext}$, for the MRN and large-grain models, with 20% oxygen in the form of ice mantles, is presented in Figure 4*a*, where it is readily apparent that, except at the shortest wavelengths, the MRN curves follow Rayleigh behavior (i.e., $\kappa_{sca} \sim \lambda^{-4}$) while the large grain curves do not. Although ice is unimportant in scattering in the MRN case, it does dominate the extinction around 3 μm. For large grains, scattering in the 3 μm ice band is much more pronounced, a direct consequence of the increase in the overall size of the icy grains (see Fig. 3). The structure around 3 μm in the scattering opacity of the

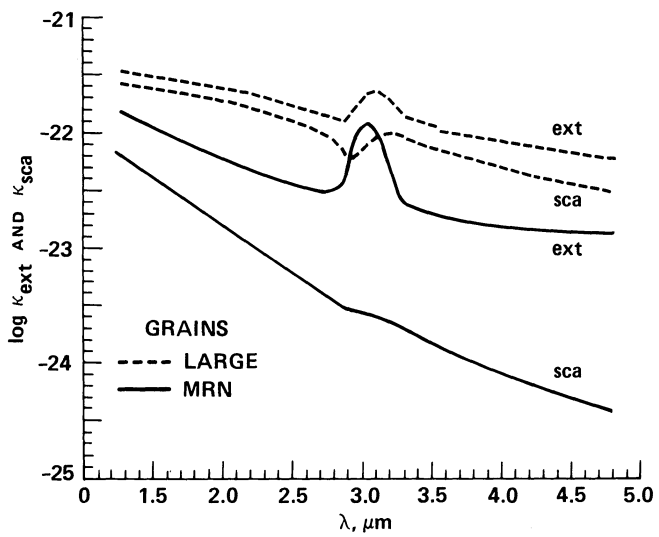

FIG. 4*a*

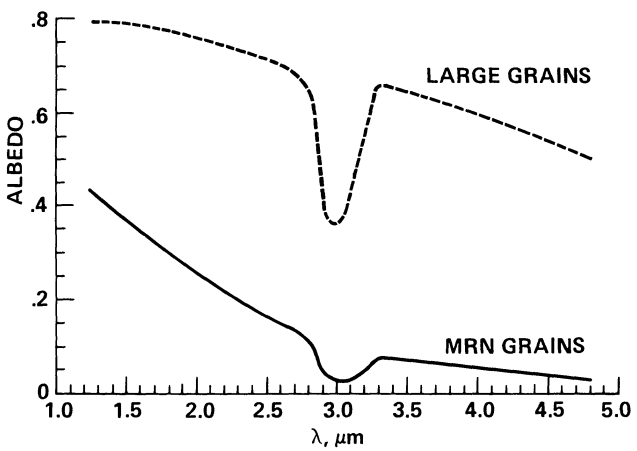

FIG. 4*b*

FIG. 4.—(*a*) Plot of the scattering and extinction opacities per hydrogen atom, κ_{sca}(cm^{-1} H^{-1}) and κ_{ext}(cm^{-1} H^{-1}), respectively. Solid lines represent the MRN model, and dashed lines represent the large grain model. Both models have ice mantles containing 20% of the available oxygen. Except at the shortest wavelengths, the MRN curves follow Rayleigh behavior ($\kappa_{sca} \sim \lambda^{-4}$), while the large-grain curves do not. Although ice is unimportant in scattering in the MRN case, it does dominate the extinction around 3 μm. For large grains, scattering in the 3 μm ice band is much more pronounced. (*b*) Plot of the grain albedo vs. wavelength for the MRN (*solid line*) and large-grain models (*dashed line*). Note that, although the ice band extinction peaks at 3.05 μm, in the albedo this is shifted to $\sim$3.0 μm. The presence of the ice has little effect far from this resonance in either scattering or extinction.

large grains directly reflects the anomalous dispersion of ice across its OH stretching resonance at 3.08 μm. Indeed, for a "soft" particle (i.e., $n \sim 1$ and $k \sim 0$), the scattering efficiency, Q_{sca}, is directly proportional to the phase lag, ρ, of the electromagnetic wave passing through the grain (Greenberg 1978) given by

$$\rho = \frac{4\pi a}{\lambda}(m - 1)\,, \tag{31}$$

so that the scattering cross section is approximately proportional to the real index of refraction, n.

The 3.08 μm ice band is much more pronounced in the extinction curve of the MRN model than in that of the large grain model. This decrease in the relative strength of the ice band is due to a decreased contrast with the continuum resulting from the increased scattering cross section of the large grains.

A comparison of the albedo for both the MRN and large-grain models with 100% oxygen is shown in Figure 4*b*. In the MRN case, extinction dominates and the albedo is generally small. For the large-grain model, the albedo is higher (due to the larger grain size) and somewhat flatter (due to the less steep wavelength dependence of scattering by the larger grains). Note also that, while the scattering cross section is proportional to λ^{-4}, the wavelength dependence of the albedo is less steep ($\sim\lambda^{-3}$).

The apparent ice bands in the albedo curves (Fig. 4*b*) differ from those in the extinction curve (Fig. 4*a*). For the MRN case, this is the result of the steep rise in the "continuum" scattering across the 3.08 μm feature, which has broadened the apparent feature considerably. In the large grain case, scattering by ice is very important in the 3 μm region (see Fig. 4*a*), resulting in a pronounced shift of the ice band to shorter wavelengths.

IV. PARAMETER SPACE STUDY

The free parameters in the model are the optical properties of the grain materials, the limits in the grain size distribution, the dust column density, the geometry, the distance from the source to the scattering location, and the intrinsic flux and spectrum of the source. The parameters adopted in our standard model, based on the Pendleton *et al.* (1986) observations of OMC-2, are given in Table 1. The distance from Earth to OMC-2 is taken to be 500 pc. In the case of OMC-2, the luminosity and effective temperature of the illuminating source, IRS 1, were well established in a previous paper (Pendleton *et al.* 1986). We adopt these results and fix the intrinsic flux and illuminating spectrum by assuming blackbody radiation from an 800 K (dusty) object with a total luminosity of 500 $L_\odot$. For simplicity, we selected an incident intensity angle (θ_0) of 0°, which means that the incident light enters perpendicular to the plane parallel slab (see Fig. 2), but this assumption is of little consequence (see § IV*d*). Several of the parameters in our standard model will be varied in turn in the following discussion.

a) Optical Depth and Source Temperature Effects

Optical depth effects in an isotropic scattering nebula have been evaluated for the three cases (optically thin, semi-infinite slab, and intermediate optical depth) discussed in § II. For the optically thin and intermediate cases, the optical depth at 1.25 μm has been set equal to 0.05 and 0.5, respectively. At other wavelengths, the optical depth is calculated according to the extinction law (see eq. [14]). The optical depth as discussed here refers to the optical depth of the slab, τ, as shown in Figure 2.

Figure 5 shows the variation of surface brightness versus wavelength for the three optical depth cases for an MRN distribution of grains observed at a scattering angle of 60°. For small optical depths the overall brightness level increases with

TABLE 1A

STANDARD MODEL PARAMETERS

Parameter	Value
Stellar Parameters:	
Luminosity	500 $L_\odot$
Radius	8.3×10^{13} cm
Temperature	800 K
Nebular Parameters:	
Distance from source to nebula, d_{neb}	5.1×10^{16} cm
Incoming angle, θ_0	0°
Outgoing angle, θ	75°

TABLE 1B

COMPARISON OF GRAIN MODELS

Parameter	MRN Grain Size Distribution[a]	Large-Grain Model[a]
Lower Limit, a_-	0.005 μm	0.225 μm
Upper Limit, a_+	0.25 μm	0.8 μm
Silicate Abundance, A_{si}	$10^{-25.16}$ cm$^{2.5}$ H^{-1}	$10^{-25.16}$ cm$^{2.5}$ H^{-1}
Carbon Abundance, A_c	$10^{-25.11}$ cm$^{2.5}$ H^{-1}	$10^{-25.11}$ cm$^{2.5}$ H^{-1}
Number of Dust Grains, n_d[b]	3.32×10^{-8} H^{-1}	2.45×10^{-12} H^{-1}

[a] Either the MRN or large-grain model was used.
[b] Calculated using eq. (23).

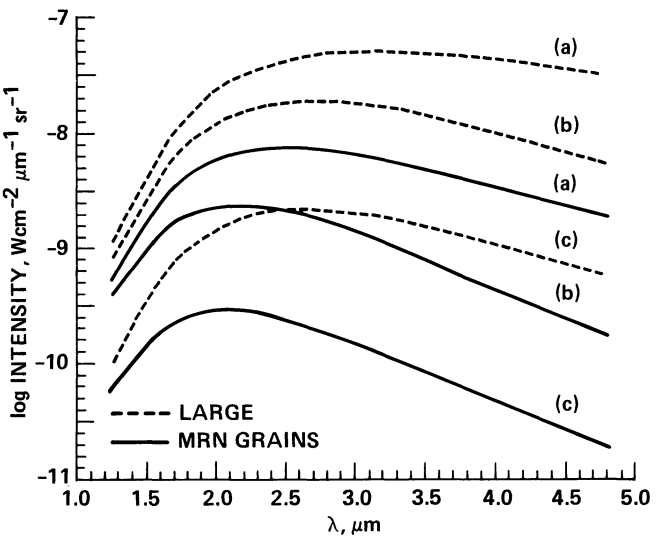

FIG. 5.—Plot of surface brightness (W cm^{-2} μm^{-1} sr^{-1}) vs. wavelength (μm) for isotropic scattering by the MRN and large-grain models, with no ice mantles, at a scattering angle of 60°, for three optical depth cases (thick, thin, and intermediate) using the standard model parameters listed in Table 1. Solid and dashed lines represent the MRN and large grain model cases, respectively. For the optically thin and intermediate cases, the optical depth at 1.25 μm was defined to be $\tau = 0.05$ and 0.5, respectively. Optical depths at all other wavelengths were calculated based on the extinction law (Fig. 4*a*). In the optically thick cases, the scattered light reflects the albedo and is independent of the column density. At low optical depths, the reflected light is proportional to the scattering optical depth.

an increase in τ_{sca} (see eq. [14]). As the optical depth becomes large, shadowing becomes important and the intensity becomes proportional to the albedo of the grains. Essentially, at low optical depths one sees all the particles, while at high optical depths only the "surface" of the nebula is seen. Note that as the optical depth increases, the shorter wavelengths become optically thick first and rapidly approach the semi-infinite slab model while the longer wavelengths are still optically thin (Fig. 5).

The assumed shape of the illuminating source (blackbody radiation at 800 K) dominates the shape of the reflected spectrum, most notably at the shorter wavelengths. For a hotter blackbody source (1500 K), the turnover in the spectrum shifts toward shorter wavelengths (Fig. 6). Adding foreground extinction to a hotter blackbody illuminating source will produce a reflected spectrum very similar to the 800 K curve (see Fig. 6).

b) Grain Size Limits

Figure 5 contains results for the large-grain model for the optically thin, semi-infinite slab, and intermediate cases. A comparison of the MRN case to the large case shows that the general shape of the curves is similar, although the flux level is higher for the large grain case, because larger particles scatter more effectively. Indeed, the average albedo is quite high ($\varpi = 0.8$ at 1.25 μm) in the large grain case.

c) Shape of the Ice Band

We investigated the effects of adding ice mantles to the MRN distribution of graphite and silicate grains. Figure 7 shows the effect of adding ice mantles which correspond to using 20% of the available oxygen (corresponding to $\Delta a = 50$ Å) to the MRN distribution of grains for the three cases of nebular optical depths. Note that a deep ice band (minimum at ~ 3.08 μm) arises naturally in regions where $\tau \geq 1$ owing to the wavelength dependence of the albedo. In the optically thin limit, the observed intensity is directly proportional to the scattering optical depth. Since most of the ice is on the small grains, which do not contribute much to the scattering, the ice band is hardly visible in the optically thin limit. The addition of foreground extinction is required to produce an ice absorption band for optically thin nebulae. As expected, the ice band increases in depth with increasing nebular optical depth. A further point is that the ice influences the reflected spectra only in the neighborhood of the 3.08 μm ice band (see the discussion on the optical properties of the adopted grain models in § III*a*). Although not shown, when the volume of the ice mantle is increased, the depth of the ice band increases as expected.

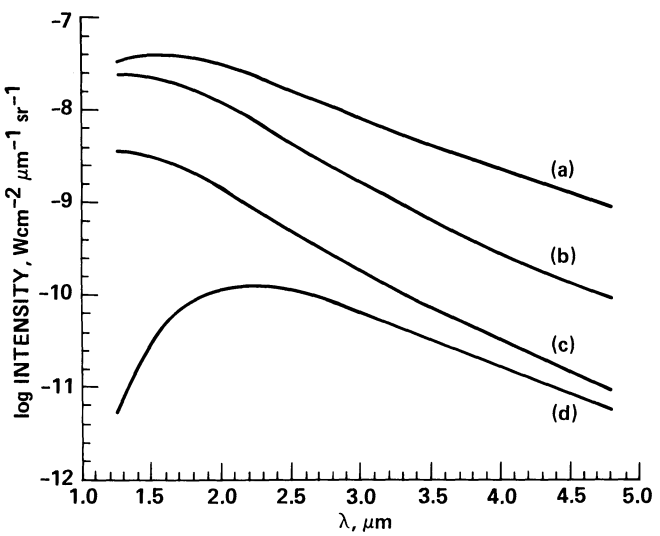

FIG. 6.—Plot of surface brightness intensity (W cm^{-2} μm^{-1} sr^{-1}) vs. wavelength (μm) for the MRN model, at a scattering angle of 60°, for an effective temperature of the illuminating source of 1500 K. All other parameters in the standard model remain unchanged. Curves (*a*), (*b*), and (*c*) represent the optically thick, intermediate, and optically thin isotropic scattering results, while curve (*d*) demonstrates the effect of adding foreground extinction [τ(2.2 μm) = 3.0] to curve (*c*). Note the resemblance in spectral shape between curve (*a*) and those shown in Fig. 5.

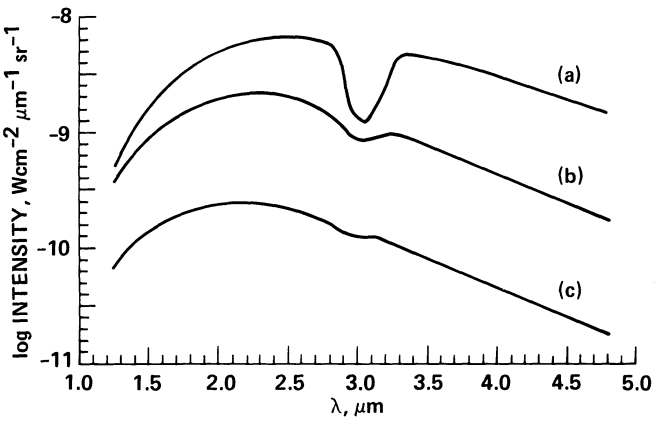

FIG. 7.—Plot of surface brightness intensity (W cm^{-2} μm^{-1} sr^{-1}) vs. wavelength (μm) for isotropic scattering by an MRN distribution of grains [$0.005 \leq a(\mu m) \leq 0.25$] with 20% oxygen in the form of H_2O ice mantles ($\Delta a = 50$ Å). Optical depth effects in the nebula are illustrated by comparison of the optically thick, intermediate, and thin curves ([*a*], [*b*], and [*c*], respectively). In the optically thin and intermediate cases, the optical depth was normalized by setting $\tau(1.25\ \mu m) = 0.05$ and 0.5, respectively.

The shape of the ice band varies dramatically between the MRN and large grain models as shown in Figures 8*a* and 8*b* for isotropic scattering by grains, which contain 100% oxygen in the form of ice mantles. In Figure 8*a*, the optically thick and optically thin MRN models are compared. The effect of scattering through the ice band is not readily apparent in either case, being masked by the absorption effects in the optically thick limit and being at a very low level in the optically thin case. Curve (*c*) demonstrates the effect of adding foreground extinction to the optically thin case. The absorption by water ice produces a minimum at 3.08 μm in this case as well as in the optically thick situation. In Figure 8*b*, a similar comparison is made between the optically thick and thin limits (curves [*a*] and [*b*]) and the addition of foreground extinction to the optically thin case (curve [*c*]) for the large-grain model. The effects of scattering by water ice mantles (i.e., the 2.9 μm feature) is quite evident in all the curves for the large-grain case. The addition of large amounts of foreground extinction shifts the ice band minimum back to 3.08 μm but leaves a pronounced wing at 2.9 μm.

We conclude, therefore, that the ice band produced in a scattering nebula differs considerably from that produced by foreground extinction. Small grains in an optically thick nebula produce broader features through the 3 μm region (relative to those produced by absorption from intervening material) with a very weak feature at 2.9 μm, while large grains always produce features around 2.9 μm. Even with large amounts of foreground extinction, this will be discernible as a wing on the 3.08 μm ice band. Thus, one telltale sign of large

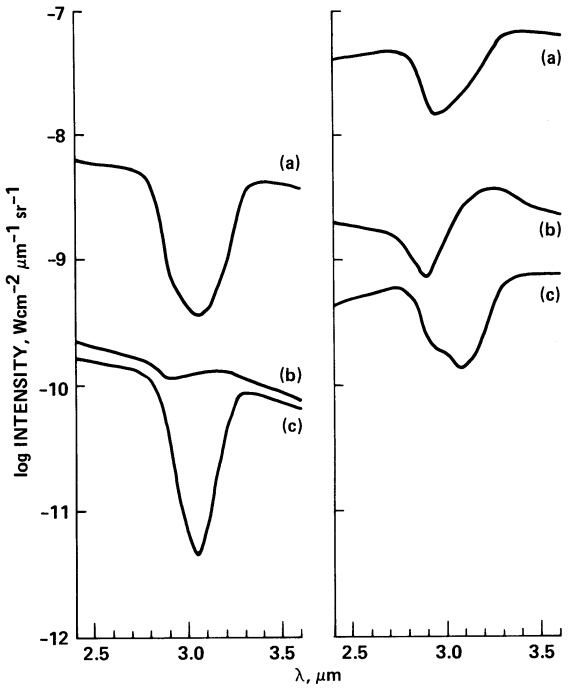

FIG. 8a FIG. 8b

FIG. 8.—Panel (*a*): plot of the shape of the 3.08 μm ice band in the reflected light by a distribution of MRN grains [$0.005 \leq a(\mu m) \leq 0.25$] with 100% oxygen in the form of ice mantles ($\Delta a = 145$ Å). Optical depth effects can be seen through comparison of the optically thick curve (*a*) to the optically thin curve (*b*). Curve (*c*) demonstrates the effect of adding foreground extinction [$\tau_c(3.1\ \mu m) = 3.0$] to curve (*b*). Panel (*b*): plot of the shape of the 3.08 μm ice band in the reflected light by a distribution of large grains [$0.225 \leq a(\mu m) \leq 0.8$] with 100% oxygen in the form of ice mantles ($\Delta a = 2600$ Å). In (*a*) and (*b*), we show results from optically thick and thin nebulae, respectively, while (*c*) represents an optically thin nebula with foreground extinction normalized such that $\tau_c(3.1\ \mu m) = 3.0$. The same dust model was used for both the nebula and foreground extinction. Note the significant differences in the shape of the ice band between the MRN grain models (*a*) and the large-grain models (*b*). This can be used as an effective probe in the determination of grain sizes in infrared reflection nebulae.

icy grains in reflection nebulae is the presence of a feature near 2.9 μm.

d) Effect of Varying the Scattering Angle

For isotropic scattering in a semi-infinite slab, all effects due to geometry (i.e., scattering angle) are contained within the $\mu_0 H(\mu)H(\mu_0)(\mu + \mu_0)^{-1}$ factor as shown in Figure 9 (see § II*a*). For our range of interest ($\omega_0 \leq 0.7$), this function varies by a factor of 2 when μ varies from 0.05 to 0.9. Note that an edge-on geometry ($\mu = 0$) is not defined within the context of a semi-infinite slab. In the optically thin case, the geometrical effects are due to the increased path length through the slab. Again, for an edge-on geometry, the intensity depends on the length of the slab, not the thickness, and is thus not defined. For an optically thin slab, the intensity is a measure of the total column density along the line of sight. For an optically thick slab, assuming $\mu = 0.5$ introduces an error of less than 25%. Conversely, this implies that the geometry cannot be easily determined from intensity measurements alone.

In realistic grain models, scattering will be nonisotropic. This introduces a second angular dependence in the intensity of the scattered light. For grains that are small compared to the wavelength of light ($2\pi a/\lambda \ll 1$), this dependence is given by the well-known Rayleigh scattering law ($C_{sca} \sim 1 + \cos^2 \phi$, where

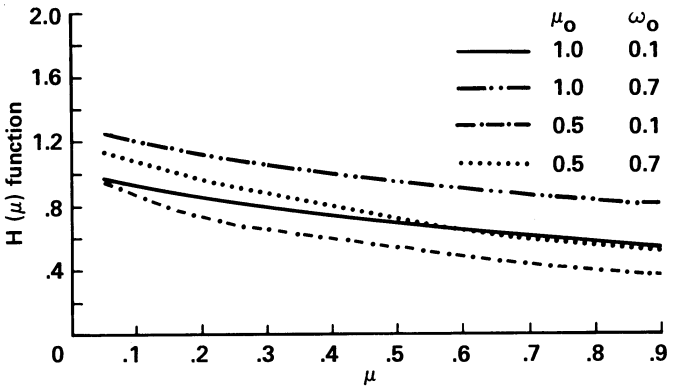

FIG. 9.—For isotropic scattering in a semi-infinite slab, all effects due to geometry are contained within the $G(\mu, \mu_0) = \mu_0 H(\mu)H(\mu_0)(\mu + \mu_0)^{-1}$ factor which is plotted here vs. μ. Four combinations of incident scattering angle, μ_0, and albedo, ω_0 are shown. This figure shows that the effect of geometry is slight for the range of interest in this work ($\omega_0 \leq 0.7$).

ϕ is the scattering angle defined as $180° - [\theta + \theta_0]$). For single scattering nebulae, this effect can be easily studied by replacing the albedo in equation (13) by $(4\pi/C_{ext})(dC_{sca}/d\Omega)$. In the optically thin limit, this results in equation (18). Figure 10 shows the differential scattering cross section for the MRN and large-

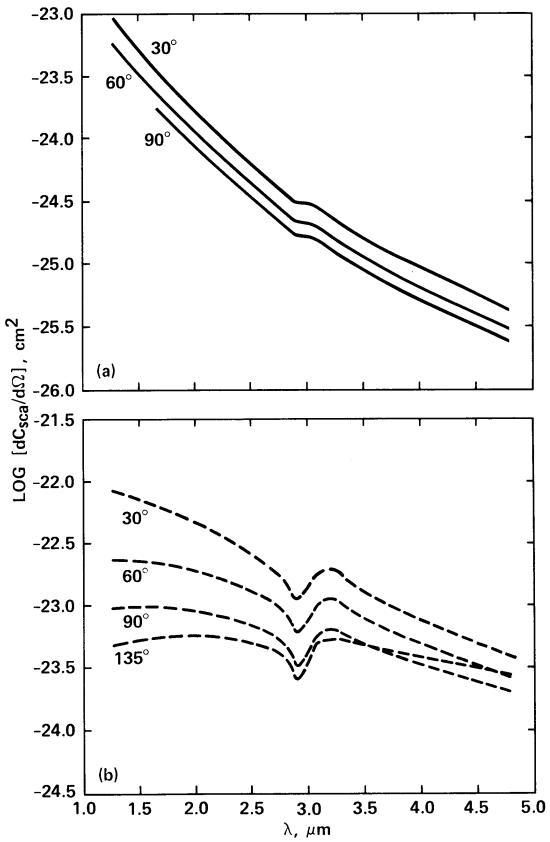

FIG. 10.—(*a*) Differential scattering cross section across the ice band for the MRN case. The three scattering angles shown (30, 60, and 90°) have very similar wavelength dependences; thus, geometry will have little effect on the shape of the ice band in the scattered light. (*b*) Differential scattering cross section across the ice band for the large-grain case. Three of the four scattering angles shown (forward scattering; $\phi = 180° - (\theta + \theta_0)$ have very similar wavelength dependences, while the backscattered curve shows that the large grains are close to the Rayleigh limit at the long wavelengths. Again, geometry will have little effect on the shape of the ice band in the scattered light.

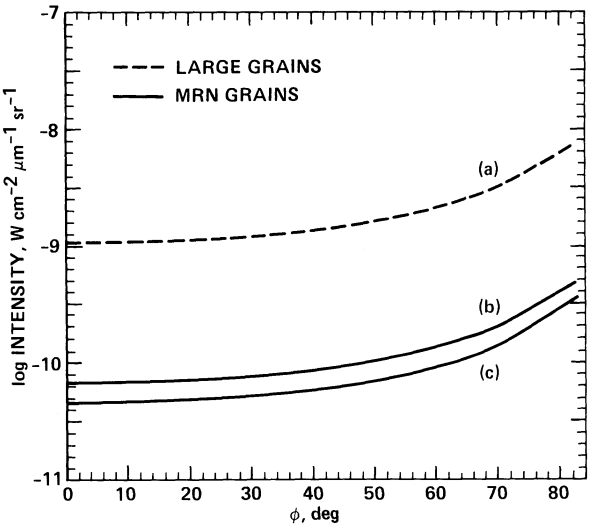

FIG. 11.—Plot of surface brightness intensity (W cm^{-2} μm^{-1} sr^{-1}) vs. ϕ (degrees) for optically thin, nonisotropic scattering. Solid and dashed lines represent an MRN and large grain distribution, respectively, with 20% oxygen in the form of H_2O ice mantles. Two wavelengths are shown in the case of the MRN grains, in the depth of the ice band (3.07 μm; curve [*b*]) and in the continuum (3.42 μm; curve [*c*]). For the large grains, these coincide (curve [*a*]). Note that most of the increase at large angles is due to the increase in column density (see Fig. 9) rather than the angular dependence of the differential scattering cross section (see Fig. 11).

grain case. The grains in the MRN model are much smaller than the wavelength in the near-infrared, and thus the scattering has a Rayleigh character (forward and backward throwing angles yield the same $dC_{sca}/d\Omega$). In contrast, in the large-grain case, scattering becomes distinctly forward throwing at the shortest wavelengths (Fig. 10*b*). This has, however, a comparatively small effect on the scattered intensity. Figure 11 shows the scattered intensity of an optically thin nebula as a function of the scattering angle ϕ for two wavelengths (the depth of the ice band and the nearby continuum). Most of the observed variations with scattering angle are actually due to the increased path length for a thin slab of constant thickness. Thus, given the other unknowns (e.g., size distribution), the isotropic assumption seems justified, except perhaps in the large-grain case at the shortest wavelengths. Figure 11 also demonstrates that the shape of the ice band, in the scattered light, will not depend on the scattering angle.

e) Polarization

Another means of distinguishing between grain sizes involves the use of polarimetry. Figure 12*a* shows that for large scattering angles ($\theta \geq 30°$), the variation of percent polarization with scattering angle is a means of distinguishing between grain sizes. The relatively small grains in the MRN model display typical Rayleigh behavior [$P(\phi) = (1 - \cos^2 \phi)(1 + \cos^2 \phi)^{-1}$; $\phi = 180° - (\theta + \theta_0)$] in that the polarization reaches nearly 100% at 90°. For the large-grain model, scattering is less Rayleigh in character, and the maximum amount of polarization is therefore considerably reduced ($\lesssim 35\%$ for the large-grain case).

The variation of polarization with wavelength for a fixed scattering angle (60°) is shown in Figure 12*b*. At the shortest wavelengths, the grains in the MRN model become comparable to the wavelength and the degree of polarization drops from that expected for Rayleigh scattering. For the large-grain model, this is true for all wavelengths shortward of 5 μm. Note the strong ice band signature in the $P(\lambda)$ curve for the large-grain model. Variations in the degree of polarization with wavelength arise because i_+ and i_- have a different phase lag dependence when the phase lag, ρ, is $\gtrsim 1$. Close to a resonance, where the index of refraction, m, varies rapidly as a function of wavelength, this shift will appear as a pronounced structure in the polarization curves. Such a shift does not occur when $\rho \leq 1$ (i.e., Rayleigh scattering), and the effects are not pronounced for the MRN case. For small scattering angles ($\theta \leq 30°$), the maximum amount of polarization is only ~20% even in the Rayleigh limit, and thus the expected differences between grain sizes may not be readily apparent at these angles.

The variation in the polarization across the ice feature is related to that in the differential scattering cross section. Both reflect changes in the scattered irradiances with wavelength (see eqs. [28] and [29]) or more precisely, with ρ. However, while the differential scattering cross section reflects the sum of the perpendicular and parallel scattering irradiances, since these irradiances are very similar in amplitude, the polarization

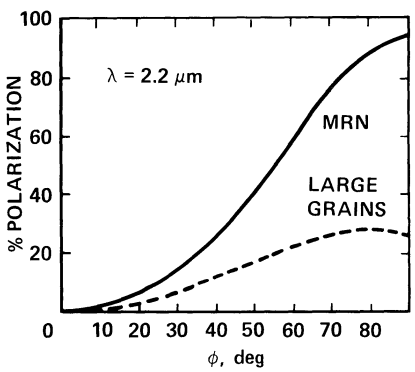

FIG. 12*a*

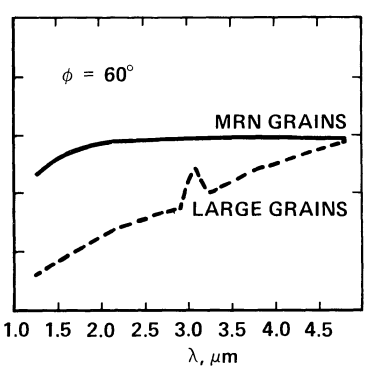

FIG. 12*b*

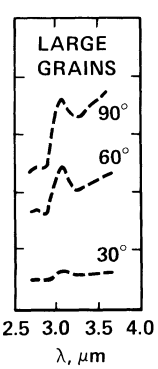

FIG. 12*c*

FIG. 12.—(*a*) Polarization vs. scattering angle for the MRN and large-grain models at 2.2 μm. MRN grains show a polarization behavior typical for the Rayleigh regime (i.e., 100% polarized at 90° and 0% polarized at 0°). In contrast, the large grains show a considerable departure from the Rayleigh behavior, and this may be another way of distinguishing between the two grain models. (*b*) Polarization vs. wavelength for the MRN and large-grain models at 60° scattering angle. Both models have 20% oxygen in the form of ice mantles on the grains (Δa = 50 and 800 Å, respectively.) Note the pronounced structure in the 3 μm region for the large grains, which may provide a diagnostic for scattering by large grains. (*c*) Polarization vs. wavelength across the ice band for the large-grain model. At all three scattering angles shown, excess polarization across the ice band is apparent above the continuum. While, as for the continuum, the peak polarization is sensitive to the geometry, the shape of this feature is not.

is actually dominated by their difference. As a result, the "ice" feature, in the differential scattering cross section and polarization curves, has a somewhat different shape (see Figs. 11 and 12*c*).

Multiple scattering within a nebula may reduce the degree of polarization somewhat. White (1979) concluded that in optically thick, plane-parallel slabs with grain albedo of ~ 0.5, the degree of linear polarization is only reduced by $\sim 20\%$ from that of single scattering. Even for an albedo of ~ 0.7 (the largest albedo in our large-grain case), the degree of polarization remains $\sim 60\%$ of the amount produced by single scattering.

V. MODELING REFLECTION NEBULA IN ORION

a) Orion Molecular Cloud 2

The infrared cluster in OMC-2 is a 2.'5 × 3.'0 region of infrared and molecular emission located about 12′ northeast of the Trapezium. Gatley *et al.* (1974) showed that at 2.2 μm, OMC-2 contains five point sources embedded in extended emission. The total far-infrared luminosity for OMC-2 is 2100 $L_\odot$ into a 3.'5 beam (Thronson *et al.* 1978). The extended emission adjacent to OMC-2 IRS 1 is the prototype of an infrared reflection nebula in a low-mass star-forming region (Pendleton *et al.* 1986). We have observed the IRS 1 region from 1–100 μm through a complementary program of photometry, polarimetry, and spectroscopy. Near-infrared photometry of three positions in the nebula located along a northeast line extending radially outward from the illuminating source, IRS 1, showed that the nebula is fairly uniform in brightness and color (Pendleton *et al.* 1986). The 3.1 μm ice feature appears in absorption in the spectra of all points observed in the nebula. The illuminating star, IRS 1, is deeply embedded in the dense and warm OMC-2 molecular cloud ($n \sim 10^5$ cm^{-3}; $T_* \sim 25$ K; Batrla *et al.* 1983). This object is likely to be a protostar. CO observations show high-velocity wings, indicative of stellar mass loss in this area (Fischer *et al.* 1985), and therefore a geometry as sketched in Figure 1 seems indicated.

The parameters in our standard model, listed in Table 1, were chosen to represent the physical parameters in the OMC-2 IRS 1 region ($L = 500\ L_\odot$; $T_* = 800$ K). For simplicity, we have used a value of $\theta_0 = 0$ and a value of $\theta = 75°$, the latter chosen to illustrate the overall fit to the intensity (see discussion below). The distance of the nebula from the source was taken to be the projected distance on the sky. As discussed in § IV*d*, geometry does not influence the shape of the reflected spectrum significantly. Of course, a change in the geometry may lead to a change in the absolute flux level through the accompanying increase in column density.

We have modeled one of the positions in the IRS 1 nebula for which we had photometry, spectroscopy, and polarimetry data. The analysis of the OMC-2 IRS 1 nebula was conducted in two parts. First, the broad-band 1–5 μm data were fitted for a position in the nebula located 5″E, 5″N of the illuminating source, IRS 1. Second, the depth of the observed ice band was fitted by varying the amount of ice on the grains.

Figure 13 compares two model fits of optically thick nebulae to observations of the OMC-2 IRS 1 nebula. The solid line represents the MRN case, while the dashed line shows results of the large grain model. The models contain 15% and 35% oxygen in the form of grain mantles, respectively. The broad-band surface brightness data for a position 5″E, 5″N of IRS 1 are shown together with 2.7–3.4 μm spectroscopic surface brightness data from the NASA IRTF cooled grating spectrometer. No additional (foreground) extinction was required to produce the fits shown in Figure 13. The figure demonstrates that the optically thick model using the MRN grain size distribution can adequately reproduce the overall shape of the energy distribution of the reflected light at the 5″E, 5″N point. However, as will be discussed below, the geometry implied by the polarization data will yield an absolute intensity which is much too small compared to the intensity observed.

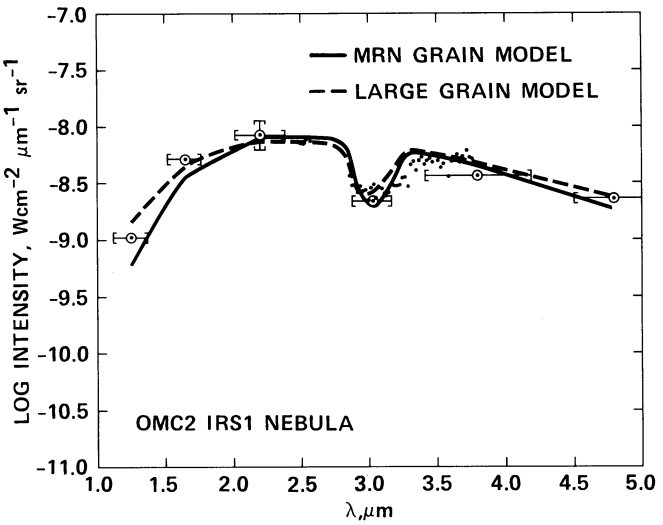

FIG. 13.—Comparison of model results with surface brightness (W cm^{-2} μm^{-1} sr^{-1}) observations of the OMC-2 IRS 1 nebula. The broad-band data for a position 5″E, 5″N of IRS 1, obtained at the NASA IRTF, are shown by open circles, with brackets denoting the wavelength coverage. A typical error bar for the broad-band points is shown for the 2.2 μm point. The spectroscopic data were obtained using the cooled grating spectrometer at the NASA IRTF. Solid and dashed lines represent isotropic scattering in an optically thick nebula assuming a distribution of MRN [$0.005 \leq a(\mu m) \leq 0.25$] and large grains [$0.225 \leq a(\mu m) \leq 0.8$], respectively. The MRN model uses 10% oxygen in the form of ice mantles ($\Delta a = 30$ Å), and the large-grain model uses 45% oxygen ($\Delta a = 1500$ Å). Note that the assumed blackbody temperature of the illuminating source (800 K for the MRN model, 1100 K for the large-grain model) is responsible for the decrease in flux at the shorter wavelengths. The projected distance on the sky from the source to the position in the nebula was used in the MRN model; a value 3 times that was used in the large grain model.

A similarly good fit to the overall shape of the intensity and depth of the ice band can be obtained for the large-grain model. Because of the slightly different wavelength dependence of albedo for the large grain model, we had to adjust the spectrum of the illuminating source to 1100 K, which is within the range of uncertainty from our observations. Also, since the absolute value of the albedo is higher in the larger grain model than in the MRN model, we have adjusted (increased) the physical distance between the star and the nebula accordingly ($d_{neb} = 1.6 \times 10^{17}$ cm). The MRN model appears to give a slightly better fit through the ice band. A small mismatch on the long-wavelength side of the ice band could be due to the presence of a low-frequency absorption wing resulting from carbonaceous impurities in the ice, a common characteristic of interstellar ices (Tielens 1989). Alternatively, this mismatch of the ice band might indicate the importance of foreground ice absorption (see Fig. 8). Note that for an optically thick nebula, the large-grain model requires more oxygen in the form of ice than does the MRN case. This merely reflects the different dependences of the albedo on the ice volume as discussed in § III*d*.

TABLE 2

MODEL RESULTS AND OBSERVATIONS FOR THREE POINTS IN THE OMC-2/IRS 1 NEBULA

Point Position[a] (E″, N″)	Polarization at 3.8 μm[b]	Scattering Angle[c] ϕ	Intensity at 3.8 μm ($\times 10^{-9}$ W cm^{-2} μm^{-1} sr^{-1})		
			Observed[b]	MRN[d]	Large Grain[d, e]
5, 5	13%	30°	3.6	0.9	7.0
8, 8	25	40	3.0	0.6	4.5
14, 14	31	45	1.7	0.2	1.8

[a] Distance of point east and north of IRS 1.

[b] Polarization errors ±2%; intensity errors <10%; beam size 6″.

[c] Scattering angle derived from polarization data using MRN or large-grain model, which give essentially the same result. Backward-scattering (180° − ϕ) angles are equally allowed.

[d] Intensity calculated for an optically thick, nonisotropic model using a star-nebula distance implied by the scattering angle.

[e] Back scattering assumed; forward scattering would result in somewhat higher intensities and might be consistent with a more optically thin model.

Table 2 contains polarization observations for three points in the OMC-2 nebula, located (5″E, 5″N), (8″E, 8″N), and (14″E, 14″N) of IRS 1. The scattering angle was derived from the polarization data based upon the two models discussed here (MRN and large-grain). Both models gave very similar scattering angles for the observed polarization. Using the true differential scattering cross section for the models and the distance to the points in the nebula (as implied by the scattering angle and the projected distance), the spatial intensity distribution has been calculated (eq. [17]) for each model (Table 2). As seen in Table 2, the MRN model fails to produce the observed intensity by a factor of ~3 at the 5″E, 5″N point and by a factor of ~10 at the 14″E, 14″N point. This is a result of the fact that the true distance to those points in the nebula is in fact greater than the projected distance, and the change in the differential scattering cross section is not significant enough to compensate for this. Therefore, since there is no way to increase the incident light by a factor of 3 (or more), the MRN model fails to reproduce the absolute intensity. A model based on larger grains ($\bar{a} \approx 50\%$ larger) will be able to reproduce the observed absolute intensity level due to the increased albedo. The large-grain model yields an absolute intensity which is slightly higher than that observed, which may merely indicate that the reflection nebula is optically thin.

Likewise, the observed dependence of the degree of polarization on wavelength also favors the large-grain model. At position (5, 5″), the measured polarization varies from 7% at 2.2 μm to 13% at 3.8 μm (Pendleton *et al.* 1986). Such variations cannot be a result of scattering by small grains, since polarization by Rayleigh scattering is independent of wavelength (see § IV*e*). Multiple scattering effects, which will be more important at the shortest wavelengths, may give rise to a (small) variation in the degree of polarization in an optically thick nebula (see White 1979). However, the low albedos for the MRN model make this an unlikely explanation. In contrast, such a variation in polarization is naturally explained by the large grain model which shows a greater variation in $P(\lambda)$ than does the MRN model (Fig. 12*b*). For example, for a scattering angle of 30° indicated by the observed polarization at 3.8 μm (Table 2), we find a degree of polarization of 9.5% and 12% at 2.2 and 3.8 μm, respectively.

In summary, we conclude that although the MRN dust model can provide as good a fit to the observed shape of the spectrum of the OMC-2 IRS 1 reflection nebula, the absolute intensity level, and the variation of the polarization with wavelength imply the presence of larger than normal dust grains ($\bar{a} \sim \lambda/2\pi \approx 0.5$ μm).

b) OMC-1

OMC-1 contains the Kleinmann-Low infrared nebula, which is considered by many to be the prototypical star-forming region. This is a region of high-mass star formation ($L \sim 10^5\ L_\odot$). Infrared continuum maps show several peaks of emission surrounded by extended emission (Rieke, Low, and Kleinman 1973; Wynn-Williams and Becklin 1974; Downes *et al.* 1981; Grasdalen, Gehrz, and Hackwell 1981). Werner, Dinerstein, and Capps (1983) showed that the extended 1–5 μm emission is due to reflection and also that some of the near-infrared continuum emission peaks are in fact produced by clumps of material which scatter light from the nearby illuminating sources. The infrared reflection nebula in OMC-1 is the brightest and most easily studied object of this type and thus is well suited for tests of the models presented here.

The 3 μm ice band has been observed at several locations in the OMC-1 reflection nebula. A comparison of small-beam (5″) and large-beam (22″) measurements of BN made by Geballe (1988) and Knacke *et al.* (1982), respectively, show that the 2.97 μm wing is much more pronounced in the large beam observations (Fig. 14), thus demonstrating the importance of scattering and the presence of large icy grains. Indeed, the large-grain model, with added foreground extinction reproduces the observed broad beam observations particularly well. Similarly, the broad 3 μm feature with the pronounced 2.9 μm wing which has been observed in the OMC-1 reflection nebula by Knacke and McCorkle (1987) is readily explained by our large-grain model (Fig. 14). The contribution of scattered light in the large-beam measurements which gives rise to the 2.9 μm feature has sometimes been identified with NH_3 impurities in the ice mantles. However, the dependence of the strength of the 2.9 μm feature on beam size (Fig. 14) strongly suggests that NH_3 is not responsible for the 2.9 μm feature. Thus, the presence of the 2.9 μm feature is a good indicator of the presence of large icy grains, making high spectral resolution of the ice band in infrared reflection nebulae a good probe of grain sizes in star formation regions. Spectropolarimetry across the ice band can test further for the presence of large grains. We emphasize that most protostars are surrounded by infrared scattering nebulae, and thus that the 2.9 μm feature observed in other objects probably also demonstrates the importance of scattering. Furthermore, we emphasize that the presence of a

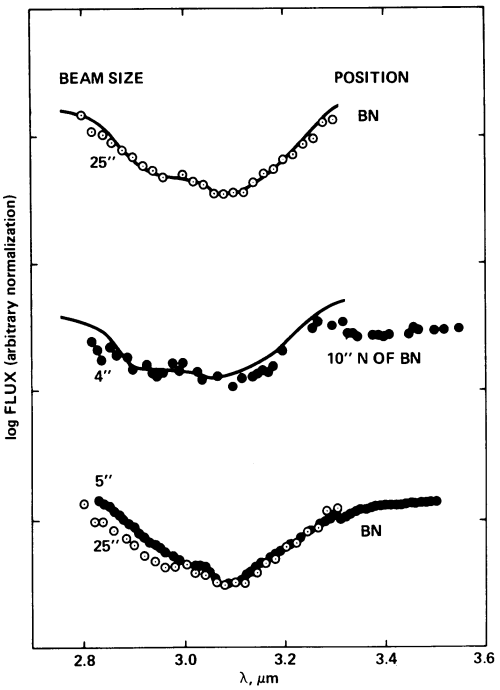

DATA FROM KNACKE et al. (1983, 1987) AND GEBALLE (1988)

FIG. 14.—Comparison of our models to two regions in OMC-1. The points in (*a*) show the ice feature in the BN object observed by Knacke *et al.* (1982) using a 25″ beam. Flux level has been adjusted arbitrarily in this comparison to highlight the differences in the shape of the ice band region. Solid line represents our model of the large grain case with 100% oxygen in the form of ice mantles and $\tau_c(3.1\ \mu m) = 3.0$. Points in (*b*) show the ice feature in a region 10″N of the BN object observed by Knacke *et al.* (1982) using a 4″ beam. Solid line represents our model of the large-grain case with 100% oxygen in the form of ice mantles and $\tau_c = 2.5$. In both models, the optical depth of the scattering nebula was normalized to $\tau(1.25\ \mu m) = 0.05$. Curve (*c*) allows comparison of two sets of BN data; open circles are data obtained using a 25″ beam (Knacke *et al.* 1982) and filled circles are 5″ data (Geballe 1988). Flux levels have been selected arbitrarily in order to demonstrate the differences in the shape of the ice band.

scattering nebula will also affect the relative strength of absorption features at different wavelengths, because the actual path length of the light may differ. For example, the column density of H_2O ice implied by the 6.0 μm OH bending mode is generally larger than that derived from the 3.08 μm OH stretching mode. A similar discrepancy exists for the observed strength of the CH stretching (3.5 μm) and deformation (6.8 μm) modes of CH_3OH (Tielens *et al.* 1989).

Rouan and Leger (1984) have analyzed the intensity and polarization of the reflected light from the scattering clump IRC-4 in OMC-1 and concluded that the scattering grains are larger than grains in the diffuse interstellar medium. The grain size derived by them is somewhat smaller than that from our analysis of the shape of the ice band. Indeed, the grain albedos derived from the observations (Werner, Dinerstein, and Capps 1983) at 2.2 and 3.8 μm, (0.4 and 0.25, respectively), fall halfway in between our MRN and large-grain cases (see Fig. 4*b*). Likewise, the observed wavelength variation of the polarization (30% at 2.2 μm and 41% at 3.8 μm; Werner, Dinerstein, and Capps 1983) is readily explained by large grains (see Figs. 12*a* and 12*b*). Alternatively, the variations in the degree of polarization with wavelength could be interpreted as a variation in the average scattering angle due to optical depth effects (Rouan and Leger 1984). However, the observed variations are so large that a highly elongated cylindrical geometry (aspect ratio 1:5) is required, which seems somewhat contrived.

The presence of large icy grains in the BN KL nebula is somewhat surprising, because previous studies of BN have concluded that the icy grains along the line of sight toward BN are small (≈1500 Å; Hagen, Tielens, and Greenberg 1983*b*). This was based on a comparison of the shape of the ice band in absorption and (dichroic) polarization. Given its large-scale polarization structure, the dichroic polarization arises in a foreground "sheet" of ice grains (Burton *et al.* 1988), which may not have grown to the same size as those in the high-density BN KL region (Tielens 1989). The dominance of smaller (ice) grains at larger distances from BN is also indicated by the relatively high continuum polarization observed (up to 40% at 3.8 μm), indicating typical sizes of the scattering grain of less than about 3000 Å. It is clear that further spectroscopic and polarimetric studies across the ice band are required to disentangle this complex source.

VI. SUMMARY

In these models of infrared reflection nebulae, a simple geometry is used in which a plane-parallel slab of material is illuminated by an infrared source. The model uses the Mathis, Rumpl, and Nordsieck (1977) power-law distribution of silicate and graphite grains which are coated with water ice, and a second, large-grain model with the same power-law slope but significantly larger grains. The largest grain core radius in the MRN model is 0.25 μm, while the largest grain core radius in the second model is 0.8 μm. Based on our parameter space study of infrared reflection nebulae and comparisons to observations, we conclude the following:

1. For isotropic scattering, in the optically thick limit the intensity follows the albedo of the grains, while in the optically thin limit the intensity is proportional to the scattering optical depth.

2. For isotropic scattering in a semi-infinite slab, all effects due to geometry are contained within a function which varies by no more than a factor of 2 for albedos ≤ 0.7. Therefore, the effects of geometry are relatively unimportant.

3. These results demonstrate that in the MRN model, the 3.08 μm ice band observed in reflection nebulae can arise from icy grains in the nebula without the aid of absorption from intervening material, as long as the nebula is optically thick. In general, the overall shape of the ice band is influenced strongly by the size of the grains and the amount of ice present. If the feature is dominated by absorption (as in the optically thick MRN case or when foreground material contributes), the ice band minimum will occur at 3.08 μm. When scattering dominates the feature, the minimum is shifted shortward to ~2.9 μm. A signature of the presence of large grains is therefore the appearance of a wing on the ice band at 2.9 μm. The presence of a scattering nebula will also affect the relative strength of absorption features at different wavelengths, such as the 3.08 and 6 μm H_2O bands and the 3.5 and 6.8 μm CH_3OH bands.

4. The overall shape of the near-infrared spectrum of the infrared reflection nebula in OMC-2 is characterized by a turnover at the shortest wavelengths owing to the spectrum of the cool illuminating source and is adequately fit by either dust grains of the order of typical interstellar grains (i.e., MRN) or larger grains ($a \sim 5000$ Å).

5. We have modeled the reflection nebulae in OMC-1 and OMC-2 and suggest that large grains ($a \sim 5000$ Å) contribute

significantly in these regions based on the presence of the 2.9 μm scattering wing on the 3.08 μm ice band in OMC-1, and on the wavelength dependence of the polarization and the absolute intensity of the scattered light in the OMC-2 nebula.

We are very grateful to our referee, John Mathis, for helpful suggestions and to Kris Sellgren for insightful discussions and aid in obtaining the data for this project. We thank the staff of the NASA Infrared Telescope Facility for their excellent support. Some of the results presented here were incorporated into the Ph.D. thesis (University of California at Santa Cruz) of Y. J. P., who would like to thank her advisor, David Rank, for his guidance and moral support throughout the thesis project. This work has benefited greatly from discussions with others working in this field, especially L. Allamandola, I. Gatley, P. Martin, S. Sandford, R. Smith, and A. Tokunaga. The research reported here has been supported by the Astrophysics Division of NASA.

REFERENCES

Abramowitz, M., and Stegun, I. A. 1970, *Handbook of Mathematical Functions* (Washington, DC: National Bureau of Standards).
Batrla, W., Wilson, T., Bastien, P., and Ruf, K. 1983, *Astr. Ap.*, **128**, 279.
Burton, M. G., Hough, J. H., Axon, D. J., Hasegawa, T., Tamura, M., McCaughrean, M. J., and McLean, I. S. 1988, *M.N.R.A.S.*, **235**, 161.
Bohren, C. F., and Huffman, D. R. 1983, *Absorption and Scattering of Light by Small Particles* (New York: Wiley).
Chandrasekhar, S. 1960, *Radiative Transfer* (New York: Dover).
Downes, D., Genzel, R., Becklin, E. E., and Wynn-Williams, C. G. 1981, *Ap. J.*, **244**, 869.
Draine, B. T. 1985, in *Protostars and Planets II*, ed. D. Black and M. Mathews (Tucson: University of Arizona Press), p. 621.
Draine, B. T., and Lee, H. M. 1984, *Ap. J.*, **285**, 89.
Fischer, J., Sanders, D. B., Simon, M., and Solomon, P. M. 1985, *Ap. J.*, **293**, 508.
Gatley, I., Becklin, E. E., Matthews, K., Neugebauer, G., Penston, M. V., and Scoville, N. 1974, *Ap. J. (Letters)*, **191**, L121.
Geballe, T. 1988, private communication.
Grasdalen, G., Gehrz, R. D., and Hackwell, J. A. 1981, in *IAU Symposium 96, Infrared Astronomy*, ed. C. G. Wynn-Williams and D. P. Cruikshank (Dordrecht: Reidel), p. 179.
Greenberg, J. M. 1978, in *Cosmic Dust*, ed. J. A. M. McDonnell (New York: Wiley), p. 178.
Greenberg, M., and Chlewicki, G. 1984, *Ap. J.*, **272**, 563.
Hagen, W., Tielens, A. G. G. M., and Greenberg, J. M. 1983*a*, *Astr. Ap. Suppl.*, **51**, 389.
———. 1983*b*, *Astr. Ap.*, **117**, 132.
Jones, A. P., Duley, W. W., and Williams, D. A. 1988, *M.N.R.A.S.*, **229**, 213.
Jura, M. 1980, *Ap. J.*, **235**, 63.
Knacke, R. F., and McCorkle, S. M. 1987, *A.J.*, **94**, 972.
Knacke, R. F., McCorkle, S. M., Puetter, R. C., Erickson, E., and Kratschmer, W. 1982, *Ap. J.*, **260**, 141.
Lenzen, R., Hodapp, K.-W., and Solf, J. 1984, *Astr. Ap.*, **137**, 202.
Mathis, J. S., Rumpl, W., and Nordsieck, K. H. 1977, *Ap. J.*, **217**, 425.
Pendleton, Y., Werner, M., Capps, R., and Lester, D. 1986, *Ap. J.*, **311**, 360.
Pendleton, Y. 1987, Ph.D. thesis, University of California at Santa Cruz.
Rieke, G. H., Low, F. J., and Kleinman, D. E. 1973, *Ap. J. (Letters)*, **186**, L7.
Rouan, D., and Leger, A. 1984, *Astr. Ap.*, **132**, L1.
Savage, B. D., and Mathis, J. S. 1979, *Ann. Rev. Astr. Ap.*, **17**, 73.
Sellgren, K. 1989, in *IAU Symposium 135, Interstellar Dust*, ed. L. J. Allamandola and A. G. G. M. Tielens (Dordrecht: Kluwer), p. 103.
———. 1984, *Ap. J.*, **277**, 623.
Thronson, H. A., Harper, D. A., Keene, J., Lowenstein, R. F., Moseley, H., and Telesco, C. M. 1978, *A.J.*, **83**, 492.
Tielens, A. G. G. M. 1989, in *IAU Symposium 135, Interstellar Dust*, ed. L. J. Allamandola and A. G. G. M. Tielens (Dordrecht: Kluwer), p. 239.
Tielens, A. G. G. M., Allamandola, L., Bregman, J., Graps, A., and Witteborn, F. 1989, in preparation.
Tokunaga, A. T., Lebofsky, M. J., and Rieke, G. H. 1981, *Astr. Ap.*, **99**, 108.
Warren, S. G. 1984, *Appl. Optics*, **23**, 1206.
Werner, M. W., Dinerstein, H. L., and Capps, R. W. 1983, *Ap. J. (Letters)*, **265**, L13.
White, R. L. 1979, *Ap. J.*, **230**, 116.
Witt, A. N. 1989, in *IAU Symposium 135, Interstellar Dust*, ed. L. J. Allamandola and A. G. G. M. Tielens (Dordrecht: Kluwer), p. 87.
Witt, A. N. 1977, *Ap. J. Suppl.*, **35**, 1.
Wynn-Williams, C. G., and Becklin, E. E. 1974, *Pub. A.S.P.*, **86**, 5.
Yamashita, T., Sato, S., Nagata, T., Gatley, I., Hayashi, S., and Fukui, Y. 1989, *Ap. J.*, **336**, 832.

YVONNE J. PENDLETON, A. G. G. M. TIELENS, and M. W. WERNER: NASA Ames Research Center, Mail Stop 245-6, Moffett Field, CA 94035